

Article

Mesoporous Nano-Sized BiFeVO_{x,y} Phases for Removal of Organic Dyes from Wastewaters by Visible Light Photocatalytic Degradation

Niyazi A. S. Al-Areqi ^{1,*},[†], Muhamad Umair ^{2,*},[†], Ahmed M. Senan ³, Ahlam Al-Alas ¹, Afraah M. A. Alfaatesh ¹, Saba Beg ⁴, Kashif-ur-Rehman Khan ⁵, Sameh A. Korma ⁶, Mohamed T. El-Saadony ⁷, Mohammed A. Alshehri ⁸, Ahmed Ezzat Ahmed ^{8,9}, Ahmed M. Abbas ^{8,10}, Riyad A. Alokab ¹ and Ilaria Cacciotti ¹¹

- ¹ Department of Chemistry, Faculty of Applied Science, Taiz University, Taiz 6803, Yemen; ahlamalalas@gmail.com (A.A.-A.); afraahmohammed35@gmail.com (A.M.A.A.); riad.aloqob@ye.liu.edu.ib (R.A.A.)
- ² Department of Food Science and Engineering, College of Chemistry and Environmental Engineering, Shenzhen University, Shenzhen 518060, China
- ³ Glycomics and Glycan Bioengineering Research Center, School of Food Science and Technology, Nanjing Agricultural University, Nanjing 210095, China; ahmedmsenan@njau.edu.cn
- ⁴ Department of Chemistry, Aligarh Muslim University, Aligarh 202002, India; profsababeg@gmail.com
- ⁵ Department of Pharmaceutical Chemistry, Faculty of Pharmacy, The Islamia University of Bahawalpur, Bahawalpur 63100, Pakistan; kashifur.rahman@iub.edu.pk
- ⁶ Department of Food Science, Faculty of Agriculture, Zagazig University, Zagazig 44519, Egypt; sameh.hosny@zu.edu.eg
- ⁷ Department of Agricultural Microbiology, Faculty of Agriculture, Zagazig University, Zagazig 44511, Egypt; m_tlatelsadony@yahoo.com
- ⁸ Department of Biology, College of Science, King Khalid University, Abha 61413, Saudi Arabia; Alshehri44@gmail.com (M.A.A.); Aabdelrahman@kku.edu.sa (A.E.A.); ahmed.abbas76@gmail.com (A.M.A.)
- ⁹ Department of Theriogenology, Faculty of Veterinary Medicine, South Valley University, Qena 83523, Egypt
- ¹⁰ Department of Botany and Microbiology, Faculty of Science, South Valley University, Qena 83523, Egypt
- ¹¹ Department of Engineering, INSTM RU, University of Rome “Niccolò Cusano”, Via Don Carlo Gnocchi 3, 00166 Roma, Italy; ilaria.cacciotti@unicusano.it
- * Correspondence: niyazi75.alareqi@gmail.com (N.A.S.A.-A.); umair@szu.edu.cn (M.U.); Tel.: +967-775-707-172 (N.A.A.-A.); +86-177-1291-5202 (M.U.).
- † These authors contributed equally to this work.

Abstract: With an increasing demand for industrial dyes in our daily lives, water conditions have become worse. Recently, the removal of such environmentally hazardous pollutants from wastewaters through photocatalytic degradation has been drawing increased attention. Three mesoporous nanophases of BiFeVO_{x,y} as ($\text{Bi}_2\text{Fe}^{\text{III}}\text{V}_{1-y}\text{O}_{5.5-y}$) visible light photocatalysts were synthesized in this study using ethylene glycol-citrate sol-gel synthesis combined with microwave-assisted calcination. X-ray diffraction (XRD), differential thermal analysis (DTA), FTIR spectroscopy, X-ray photoelectron spectroscopy (XPS), scanning electron microscopy coupled with energy dispersive X-ray spectrometry (SEM-EDS), nitrogen adsorption-desorption isotherms, and UV-Vis diffuse reflectance spectrophotometry (UV-Vis/DRS) were used to characterize the BiFeVO_{x,y} photocatalysts. The visible light-induced photocatalytic activities of the BiFeVO_{x,y} phases were evaluated by the degradation of methylene blue (MB) dye in aqueous solution at pH ~10.0. The results of this study show that the combination of doping strategy with the utilization of advanced synthesis methods plays an important role in improving the structure and surface properties of BiFeVO_{x,y} phases, and thereby enhancing their adsorption and photocatalytic efficiencies. The synthesized mesoporous tetragonal γ -BiFeVO_{x,y} nanophase has been proven to be a potential visible-light photocatalyst for the degradation of organic dyes.

Keywords: BiFeVO_x; photocatalyst; mesopores; dye degradation; waste water; photodegradation; adsorption



Copyright: © 2022 by the authors. Licensee MDPI, Basel, Switzerland. This article is an open access article distributed under the terms and conditions of the Creative Commons Attribution (CC BY) license (<https://creativecommons.org/licenses/by/4.0/>).

1. Introduction

Synthetic dyes comprise an important part of industrial water effluents as they are discharged in abundance by many manufacturing industries. The impact of these dyes on the environment is a major concern because of the potentially carcinogenic properties of these chemicals [1–6]. Many treatment methods have been recently developed and applied to remove these dyes from wastewater, such as adsorption, ultrafiltration, reverse osmosis, coagulation, and ion exchange [7–13]. However, such methods do not result in the destruction of the dye molecules [14–17]. Therefore, much attention has been paid to finding an alternative to conventional methods such as “advanced oxidation processes” (AOPs), which are based on the chemical, photochemical, and photocatalytic production of hydroxyl radicals (OH^\bullet), which act as strong oxidizing agents for the degradation of organic dyes [18]. The advantages of AOPs over competing processes are: complete mineralization; no waste disposal problem; low cost; and only mild temperature and pressure conditions [19–22]. Many metal oxides, such as TiO_2 , ZnO , ZrO_2 , and so forth, have been widely investigated in the AOPs for the photodegradation of synthetic dyes in wastewater [20,23–25]. However, because of their relatively high band-gap energy, they are activated only by ultraviolet light absorption [26,27], which limits their commercial application for water and wastewater treatment. To overcome this problem, the visible light-induced photocatalysts are required to apply the AOPs more efficiently and to degrade these dyes using viable sunlight energy.

Our previous research on the electrical properties of oxide–ion conductors, namely $\text{BiMeVO}_{\text{x.y}}$ (Bi = bismuth, Me = dopant metal ion, V = vanadium, Ox = oxide, and y = molar dopant concentration), derived by the partial substitution of Me for V in the parent compound, $\text{Bi}_2\text{VO}_{5.5}$, of a layered Aurivillius-type structure, discovered that many BiMeVO_{x} materials behave as semiconductors at temperatures less than $300\text{ }^\circ\text{C}$ [28–32]. The first attempt to employ such types of materials as visible light photocatalysts was made by Thakral and Uma [33] by investigating the visible light photocatalytic efficiencies of $\text{Bi}_2\text{VO}_{5.5}$ and its substituted analogues, i.e., BiAlVO_{x} , and BiGaVO_{x} , for the degradation of methylene blue (MB) in aqueous media. These were found to be moderate for MB photodegradation, and showed similar activities of Bi_2AlVO_7 and Bi_2GaVO_7 photocatalysts [17]. Another investigation was also carried out with the BiNiVO_{x} analogue on the photodegradation of a synthetic azo dye [34–36], which showed a considerably high photocatalytic efficiency, even though it was synthesized via the conventional solid-state reaction. Moreover, a possible photocatalytic degradation mechanism was proposed, and clearly presented. However, Chen et.al. [37] studied the photocatalytic activities of hierarchical $\text{Bi}_2\text{VO}_{5.5}$ hollow microspheres synthesized by the solvothermal route for the photodegradation of rhodamine-B (RhB), finding them to be much higher compared to other $\text{Bi}_2\text{VO}_{5.5}$ powders prepared by conventional synthesis routes.

Although some doped $\text{Bi}_2\text{VO}_{5.5}$ materials have shown enhanced photocatalytic efficiencies for the degradation of some organic dyes within the visible light spectral range as a consequence of band gap narrowing, there is no clear, convincing evidence to realize an actual relationship between the phase stability, nanostructure and photocatalytic efficiency of BiMeVO_{x} photocatalysts [38,39]. So, in this paper, we report another new member of the $\text{BiMeVO}_{\text{x.y}}$ family, viz., $\text{BiFeVO}_{\text{x.y}}$, $\text{Bi}_2\text{Fe}^{\text{(III)}}_{\text{y}}\text{V}_{1-\text{y}}\text{O}_{5.5-(3\text{y}/2)}$, used for the photocatalytic degradation of MB dye under visible light irradiation. This study was devoted to carefully investigating the influence of metal doping on the phase stability and photocatalytic properties of the $\text{BiFeVO}_{\text{x.y}}$ photocatalyst, to provide a more detailed investigation on the correlation of the enhanced photocatalytic efficiencies with the nanostructured $\text{BiFeVO}_{\text{x.y}}$ phases porosity.

Three mesoporous nanophases (α -monoclinic, β -orthorhombic, and γ -tetragonal) of $\text{BiFeVO}_{\text{x.y}}$ were prepared by means of ethylene glycol-citrate sol-gel synthesis followed by microwave-assisted calcination. In this investigation, sophisticated analytical methods, such as X-ray diffraction (XRD), differential thermal analysis (DTA), Fourier transform infrared spectroscopy (FTIR), X-ray photoelectron spectroscopic (XPS), scanning electron microscopy (SEM), energy dispersive X-ray spectrometry coupled with scanning electron

microscopy (EDS-SEM), nitrogen adsorption equipment and UV-Vis diffuse reflectance spectra (UV-Vis/DRS), were used.

2. Materials and Methods

2.1. Experimental

Preparation of BiFeVO_{x,y} Phases

Analytical grade Bi(NO₃)₃.5H₂O, NH₄VO₃ and Fe(NO₃)₃.9H₂O (Sigma Aldrich, St. Louis, MO, USA) were used as starting materials without any further purification. In the present study, three different phases (α -monoclinic, β -orthorhombic, and γ -tetragonal) of BiFeVO_{x,y} were prepared at three different compositions, $y = 0.03$, $y = 0.07$, and $y = 0.15$, respectively. It is interesting to note that the three main crystallographic phases of BiFeVO_{x,y} were found to be effectively stabilized with a high purity at these dopant concentrations. Stock solutions of the starting materials (0.1 M) were prepared by dissolving an accurately weighed amount of corresponding material in deionized water. A 0.2 M citric acid (Sigma Aldrich, St. Louis, MO, USA) solution used as chelating agent was prepared in a deionized water–ethylene glycol mixture at a volumetric ratio of 3:1. A 0.5 M NH₃ (Sigma Aldrich, St. Louis, MO, USA) solution was also used for adjusting the pH. The starting material's solutions were mixed at a volumetric ratio of 2:y:(1 – y) = Bi:Fe:V with citric acid solution to form sol solutions. The ratio of citric solution to total metal ions was set at 1.5:1.0. The resulting sol solutions' pH values were adjusted to ~7 by adding ammonia solution. The sol solutions were then heated at 80 °C under constant stirring for two hours to form visible gel. The conditions (Temperature and time) were established according to our previous work reported for another member of the BiMeVO_x family that was synthesized by the same sol-gel route [40]. Wet gels were further dehydrated in an oven at 90 °C for 12 h to remove the excess water and obtain dried xerogels. The xerogel was thoroughly mixed in an agate mortar for further homogenization and was then subjected to a microwave-assisted calcination for 30 min in a modified microwave oven operated at a frequency of 2.45 GHz.

2.2. Characterization of Photocatalyst Samples

The phase structure of as-prepared BiFeVO_{x,y} photocatalysts was investigated by XRD using a Rigaku/Max-B X-ray diffractometer (Rigaku Corporation, Tokyo, Japan) with Ni-filtered CuK α radiation ($\lambda = 1.54060 \text{ \AA}$). Data were recorded with the Bragg–Brentano geometry at a scan time of 0.6 s/increment in the range $5^\circ \leq 2\theta \leq 90^\circ$. The unit cell parameters were calculated by the Rietveld refinement method using the X' Pert Plus software program. The average crystallite size was calculated from XRD line broadening via the Scherrer equation: $D = 0.89\lambda/B \cos\theta$, where D is the crystal size in nm, λ is the CuK α radiation wavelength ($\lambda = 1.54060 \text{ \AA}$), B is the half-width of the peak in radians and θ is the corresponding diffraction angle.

The DTA measurements were carried out with a Schimatzu SC-TA 60 thermal analyzer. A 20 mg-powdered sample of BiFeVO_{x,y} was heated from 40 °C to 1000 °C at a constant heating rate of 10 °C min⁻¹. The experiments were run in a nitrogen atmosphere supplied at a flow rate of 100 mL min⁻¹.

The FTIR spectra of the synthesized compositions were collected on a Perkin Elmer spectrophotometer (PerkinElmer®, Waltham, MA, USA) in the transmittance mode over the wavenumber range of 4000–400 cm⁻¹. BiFeVO_{x,y} powders were diluted equally well with analytical grade KBr to 1.5 w/w%.

The XPS analysis of BiFeVO_{x,y} phases was performed on a VG-ADES 400 instrument with MgK α ($h\nu = 1253.6 \text{ eV}$) as the excitation source. A powdered sample of BiFeVO_{x,y} was pre-treated in an O₂ flow of 30 mL min⁻¹ for 1 h at 500 °C, and was then outgassed for 30 min before being analyzed. The C 1s signal at 284.6 eV was taken as a reference for the binding energy calibration.

The morphologies and microstructures of the as-prepared photocatalysts were examined by scanning electron microscopy using a JEOL-6510 LV SEM (JEOL Ltd., Tokyo, Japan); the ImageJ program was employed for processing the reacquired SEM micrographs and

calculating the average particle sizes. From energy dispersive X-ray spectrometry (EDS) coupled with the SEM instrument, the corresponding EDS profiles scanned over a full scale up to 20 kV were also taken for investigating the elemental compositions of the samples' surfaces and checking their purity.

The nitrogen adsorption–desorption isotherms were collected in the nitrogen partial pressure range of $0.01 \leq (P/P_0) \leq 0.99$, by means of an Autosorb-1 (Quantachrome, Boynton Beach, FL, USA) adsorption at 77 K. The specific surface areas were calculated using the Brunauer–Emmett–Teller (BET) method, while the BJH model was applied for the pore size distribution.

The optical band-gap energy [41] of the as-prepared photocatalyst samples was estimated using the UV-Vis/DRS (Shimadzu, Tokyo, Japan). Spectral data were collected on a Shimadzu Scan UV-Vis spectrophotometer (UV-2450) at room temperature in the wavelength range 200–800 nm using BaSO₄ as a standard reflectance reference. The direct band-gap energy values were determined by extrapolating the straight portion of $(\alpha h\nu)^2$ vs. $(h\nu)$ plots to $\alpha = 0$ point, by means of line-regression fitting to the Kubelka–Munk Equation (1) near the band-gap edge of absorption:

$$(\alpha h\nu)^2 = A(h\nu - E_g) \quad (1)$$

where α , h , ν and A are the absorption coefficient, Planck constant, light frequency and absorption constant, respectively.

2.3. Dark Adsorption Measurements

Continuous adsorption equilibrium experiments were carried out to investigate the de-colorization of MB solution by BiFeVO_{x.y} photocatalysts in the dark. A 200 mg BiFeVO_{x.y} sample was transferred into a 500 mL, 5.0×10^{-5} M MB solution at pH ~10.0 (adjusted with diluted aqueous solutions of NH₃ and HCl). The resulting solution was magnetically stirred in the dark at a moderate speed and then allowed to sediment. At various time intervals, a 5 mL aliquot of the dye-photocatalyst suspension was centrifuged and the remaining dye concentration was determined using a Shimadzu UV-Vis spectrophotometer (UV-2450) at a maximum absorption wavelength ($\lambda_{\text{max}} = 665$ nm). The amount of MB adsorbed per unit mass of the photocatalyst at any time (q_t (mg g⁻¹)) was calculated using Equation (2):

$$q_t = \frac{V(C_0 - C_t)MW}{m} \quad (2)$$

where C_0 and C_t are the initial and remaining concentrations of the MB solution, MW the molecular mass of MB (319.85 g mol⁻¹; C₁₆H₁₈ClN₃S), m the mass expressed in grams of the BiFeVO_{x.y} photocatalyst added into a definite volume, and V the volume of the dye solution. The amount of MB adsorbed per unit mass of the photocatalyst at equilibrium (q_{max}) and the equilibrium concentration of MB (C_e) are equal to q_t , and C_t , respectively, at the adsorption equilibrium time.

2.4. Photocatalytic Degradation Measurements

The same amount of the BiFeVO_{x.y} photocatalyst and of the volume of virgin MB solution at the same conditions were transferred into a 750 mL photoreactor, equipped with water refrigeration, magnetic stirrer, and air mini pump. The resulting suspension was then magnetically stirred in the dark for 25 min to reach the adsorption–desorption equilibrium. A 300-W xenon lamp, located beyond an optical glass cut-off filter, was used as the visible light source with wavelengths greater than 400 nm. The irradiation source was located 25 cm above the surface of liquid in the photoreactor. The temperature of the reaction system was kept at 25 °C using flowing cool water in order to prevent the thermal catalytic reaction effect. At equal time intervals of irradiation (10 min), 5 mL aliquot of the reaction mixture was withdrawn from the photoreactor and then centrifuged. The dye concentration versus irradiation time was determined by measuring the maximum

absorbance at $\lambda_{\max} = 665$ nm using a Shimadzu UV-Vis spectrophotometer (UV-2450). The photocatalytic degradation percentage ($PD\%$) of MB after 120 min of irradiation was calculated using the relation (3):

$$PD\% = \left(1 - \frac{C'_t}{C_e}\right) \quad (3)$$

where C_e and C'_t are the equilibrium concentration and the concentration at irradiation time (t) of the MB solution, respectively. The photocatalytic activity of the BiFeVO_{x,y} phases for the MB photodegradation was also investigated using the pseudo first-order kinetic model (4):

$$PD\% = \ln\left(\frac{C_e}{C'_t}\right) = k_{app}, \quad (4)$$

where k_{app} denotes the apparent first-order rate constant.

3. Result and Discussion

Figure 1 presents the XRD patterns of the as-prepared BiFeVO_{x,y} systems, identifying three principal crystallographic phases: the α -(monoclinic), β -(orthorhombic) and γ -(tetragonal) BiFeVO_{x,15} phases. The α -and β -phases with space group Aba2 and Acam are assigned to BiFeVO_{x,03} and BiFeVO_{x,07}, respectively.

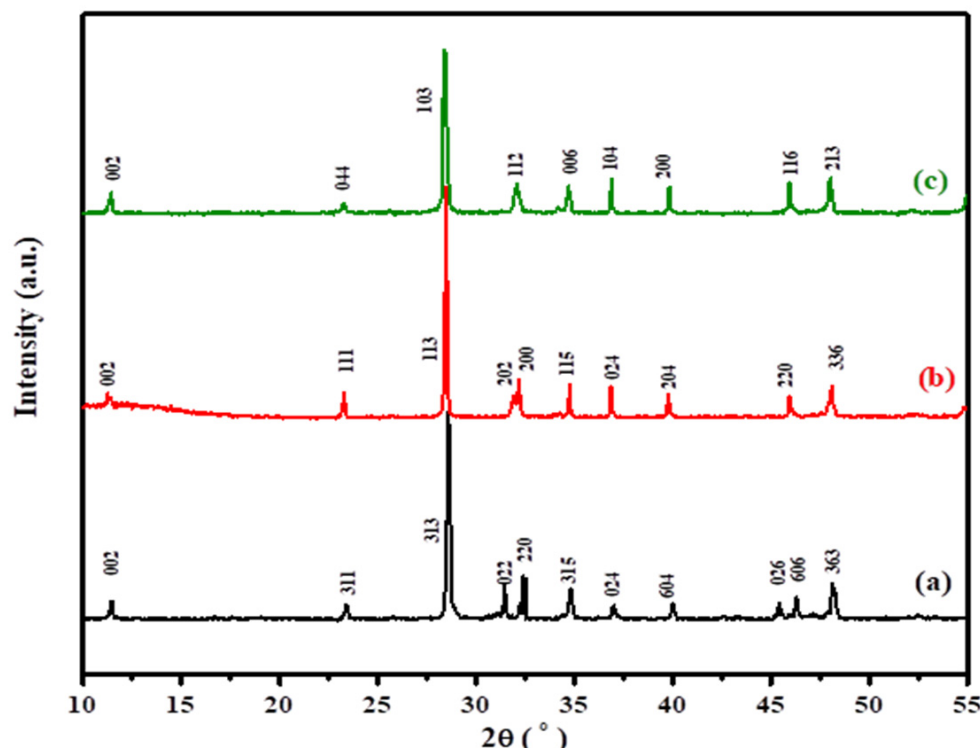


Figure 1. XRD patterns of the as-prepared BiFeVO_{x,y} systems for (a) $y = 0.03$, (b) $y = 0.07$, and (c) $y = 0.15$.

The singlet (112) sublattice peak at $2\theta \sim 32.5^\circ$ is clear evidence for the room temperature stabilization of the tetragonal γ -BiFeVO_{x,15} phase. The values of refined unit cell parameters, crystallite size (D) and crystallographic density (d_{XRD}) are summarized in Table 1. It can be observed that the lattice dimensions, particularly along the c-axis, remarkably increase with the Fe content (y). This is in fact attributed to the substitution of the smaller V⁵⁺ (0.54 Å) with the larger Fe³⁺ ion (0.78 Å) in the 6-coordination environment, adapted by the perovskite vanadate layers [42].

Table 1. Stabilized phase, refined unit cell parameters, crystallite characteristics of as-prepared BiFeVO_{x,y} photocatalyst series.

<i>y</i>	Stabilized Phase		Unit Cell Parameters			Crystallite Parameters	
	Phase	Space Group	<i>a</i> (Å)	<i>b</i> (Å)	<i>c</i> (Å)	<i>D</i> (μm)	<i>d</i> _{XRD} (g cm ³)
0.03	α	<i>Aba</i> 2	5.538	5.596	15.338	1.93	6.56
0.07	β	<i>Acam</i>	5.614	5.514	15.362	2.04	6.52
0.15	γ'	<i>I4/m mm</i>	3.971	-	15.416	1.87	6.48

The endothermic peaks shown in the DTA thermograms of the BiFeVO_{x,y} system (Figure 2) are in good agreement with the XRD assignment. Like α-Bi₂VO_{5.5} [43] and α-BiMeVOxes [44,45], α-BiFeVO_x.03 exhibited two typical endothermic peaks at 459.7 and 560.4 °C due to the successive α → β → γ' (high-temperature fully disordered tetragonal) transitions, while the single peaks observed for BiFeVO_x.07 and BiFeVO_x.15 can be ascribed to β → γ' and γ → γ', respectively.

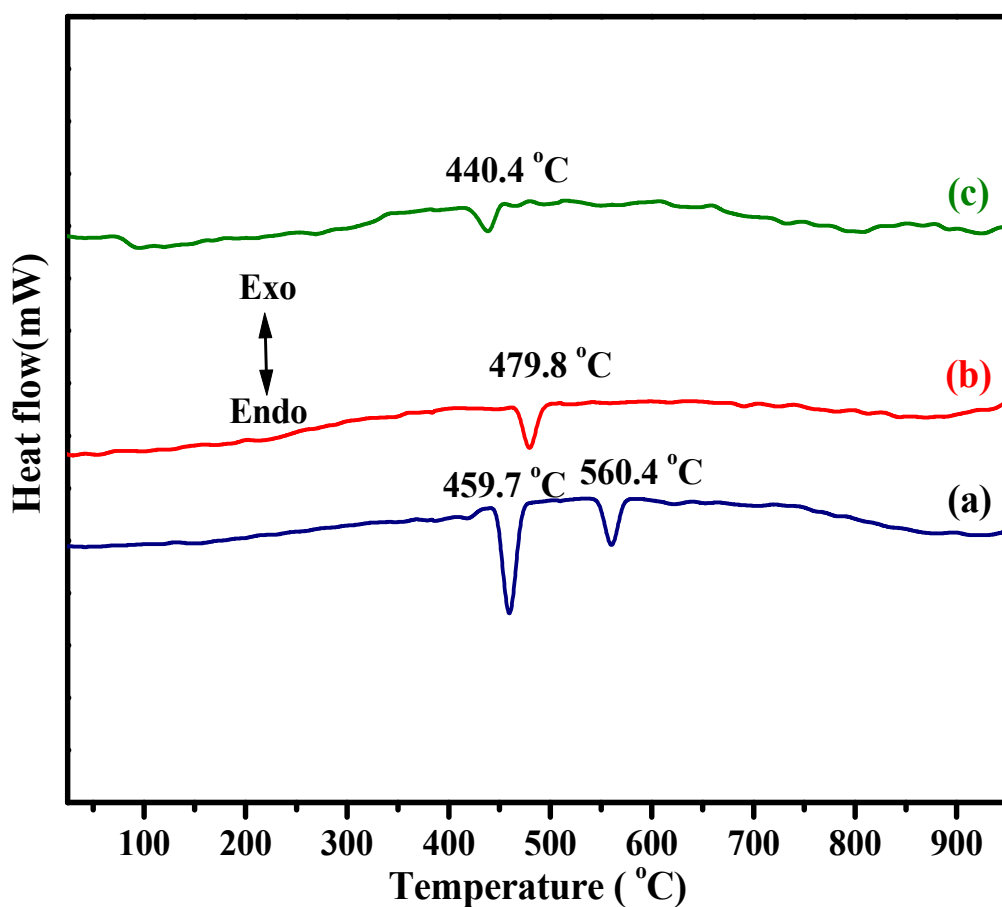


Figure 2. DTA thermograms of BiFeVO_{x,y} for (a) *y* = 0.03, (b) *y* = 0.07, and (c) *y* = 0.15.

FTIR spectra of the as-prepared BiFeVO_{x,y} compositions (Figure 3) show absorption bands in the regions 700–720, 800–990, and 510–620 cm⁻¹ which are assigned to symmetric ν_s(V-O), and asymmetric ν_{as}(V-O) stretching modes of vibration, and asymmetric deformation modes of bending δ_{as}(O-V-O) for the vanadate layers, respectively. Moreover, another band can be observed at ~460 cm⁻¹, ascribed to Bi/Fe-O stretching vibrations. Similar typical FT-IR assignments have also been reported for other BiMeVOxes prepared via the conventional solid synthesis [46].

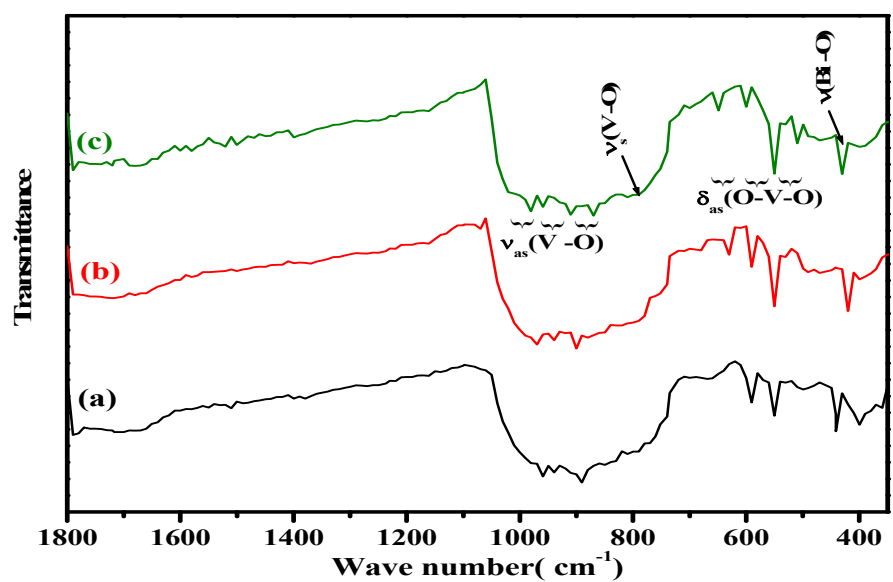


Figure 3. FTIR spectra of $\text{BiFeVO}_{\text{x.y}}$ for (a) $y = 0.03$, (b) $y = 0.07$, and (c) $y = 0.15$.

Figure 4 illustrates XPS profiles of the three $\text{BiFeVO}_{\text{x.y}}$ phases. All peaks shown here are assigned to Bi, V, Fe, and O atoms as the main surface species of as-prepared $\text{BiFeVO}_{\text{x.y}}$ compositions with single oxidation states of +3, +5, +3, and -2, respectively. XPS analysis confirms that the $\text{BiFeVO}_{\text{x.y}}$ compositions are of high purity and free of any carbon contamination and, thus, exist in single phases as already revealed by XRD results. It is interesting to note that the slight shifts in XPS peaks corresponding to angular $\text{V}2\text{p}$ and spin $\text{V}2\text{s}$ momentum towards higher binding energies with increasing Fe content are mainly caused by the partial substitution of Fe for V in the perovskite vanadate layers.

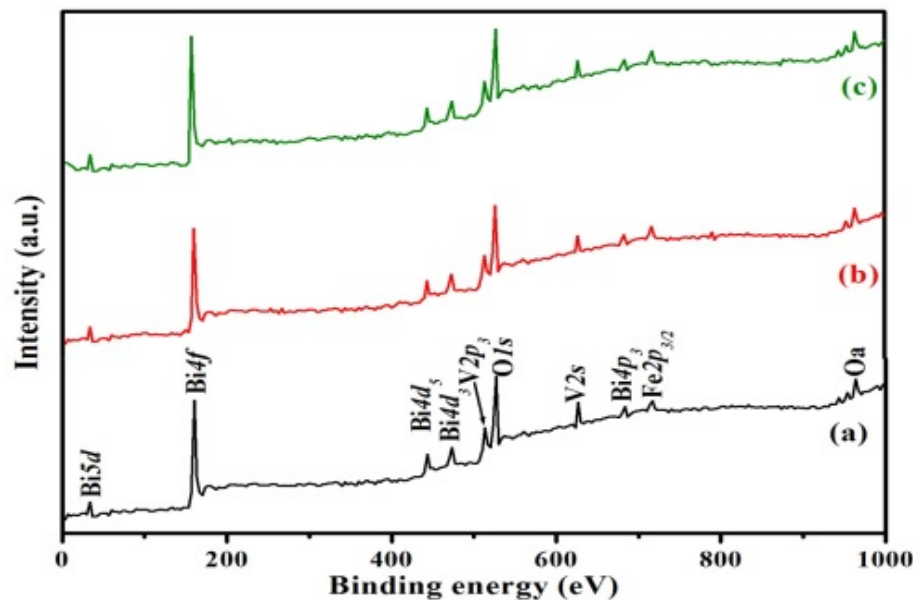


Figure 4. XPS profiles of $\text{BiFeVO}_{\text{x.y}}$ for (a) $y = 0.03$, (b) $y = 0.07$, and (c) $y = 0.15$.

However, the very small differences between the atomic percentages of O and V obtained from the XPS results (Table 2), and those theoretically deduced from the corresponding formulas are in good agreement with the fact that such materials are oxygen deficient and that the oxygen vacancies are entirely located in the vanadate layers [39,47], i.e., $[\text{V}_{1-y}\text{Fe}_y\text{O}_{3.5-y-\delta}]^{2n-} \square_\delta \frac{2n-}{n}$, where \square and δ stand for an oxygen vacancy and its molar

ratio. Moreover, the strong peak, with two little overlapped shoulders ascribed to the O1s spin momentum, indicates three different oxygen environments in the crystal structure. In detail, the strong peak is associated with the bismuthate layers ($[\text{Bi}_2\text{O}_2]^{2n+}_n$), whereas the two shoulders correspond to apical and equatorial oxygen atoms in the perovskite vanadate layers, having two principal types of Fe/V polyhedral, i.e., distorted tetrahedra and distorted octahedra. This is in a good agreement with the previous detailed studies reported for the crystal defect structure determinations of $\text{BiMeVO}_{x,y}$ [48,49].

Table 2. Chemical analysis and microstructure characteristics of the as-prepared $\text{BiFeVO}_{x,y}$ photocatalyst series.

<i>y</i>	XPS (Atomic%)					$\bar{d}(\text{nm})$	SEM Fe/V Mole Ratio
	Bi%	V%	Fe%	O%			
0.03	23.61	11.46	0.35	64.57		337.65	0.0302
0.07	23.72	11.05	0.83	64.39		308.91	0.0747
0.15	23.95	10.20	1.80	64.05		306.32	0.1762

SEM micrographs and the related EDS profiles of as-synthesized $\text{BiFeVO}_{x,y}$ phases are presented in Figure 5. It can be observed that the major particles of all samples exhibit a spherical-like shape, while the minor very tiny particles of irregular shapes are spread out at the boundaries of the spherical particles. The size distribution of spherical particles (\bar{d}) was measured to be several hundreds of nanometers (Table 2). Interestingly, the values of the Fe/V molar ratio estimated by the EDS analysis well match with those obtained from the XPS results.

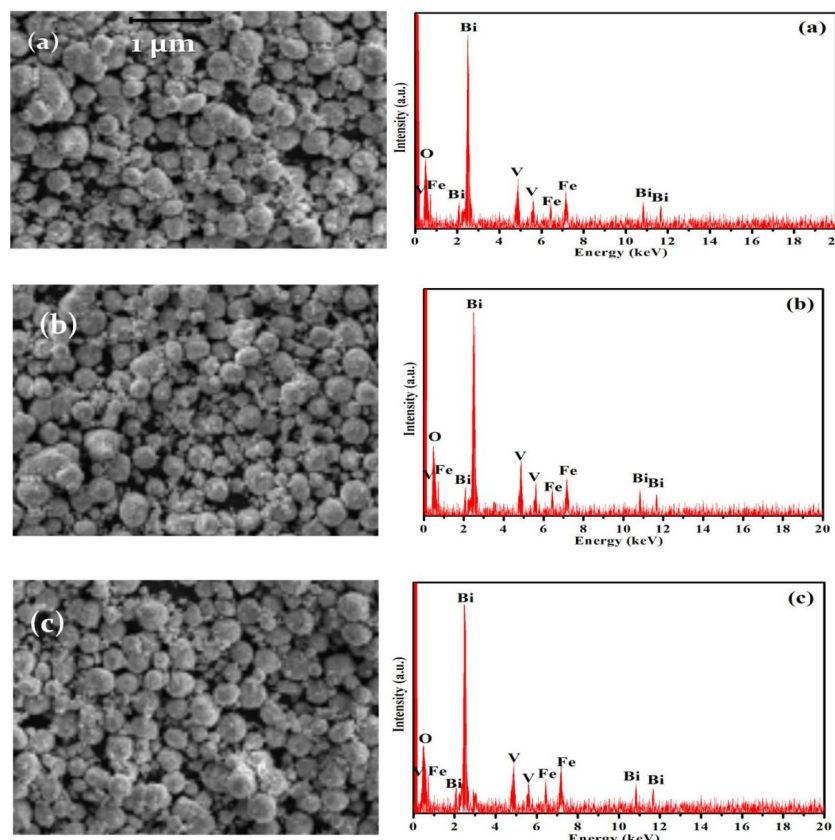


Figure 5. SEM micrographs (left) and EDS profiles (right) of $\text{BiFeVO}_{x,y}$ for (a) $y = 0.03$, (b) $y = 0.07$, and (c) $y = 0.15$.

N_2 adsorption–desorption isotherms and BJH pore size distribution curves of $\text{BiFeVO}_{\text{x.y}}$ phases are shown in Figure 6. According to the IUPAC classification, the adsorption isotherms are all of type IV with a remarkable hysteresis loop upon the desorption run. This is a typical feature of powders containing disordered mesopores finely intra-aggregated within the major spherical particles [50,51]. It is also observed that all three phases exhibit a narrow pore size distribution with a characteristic maximum.

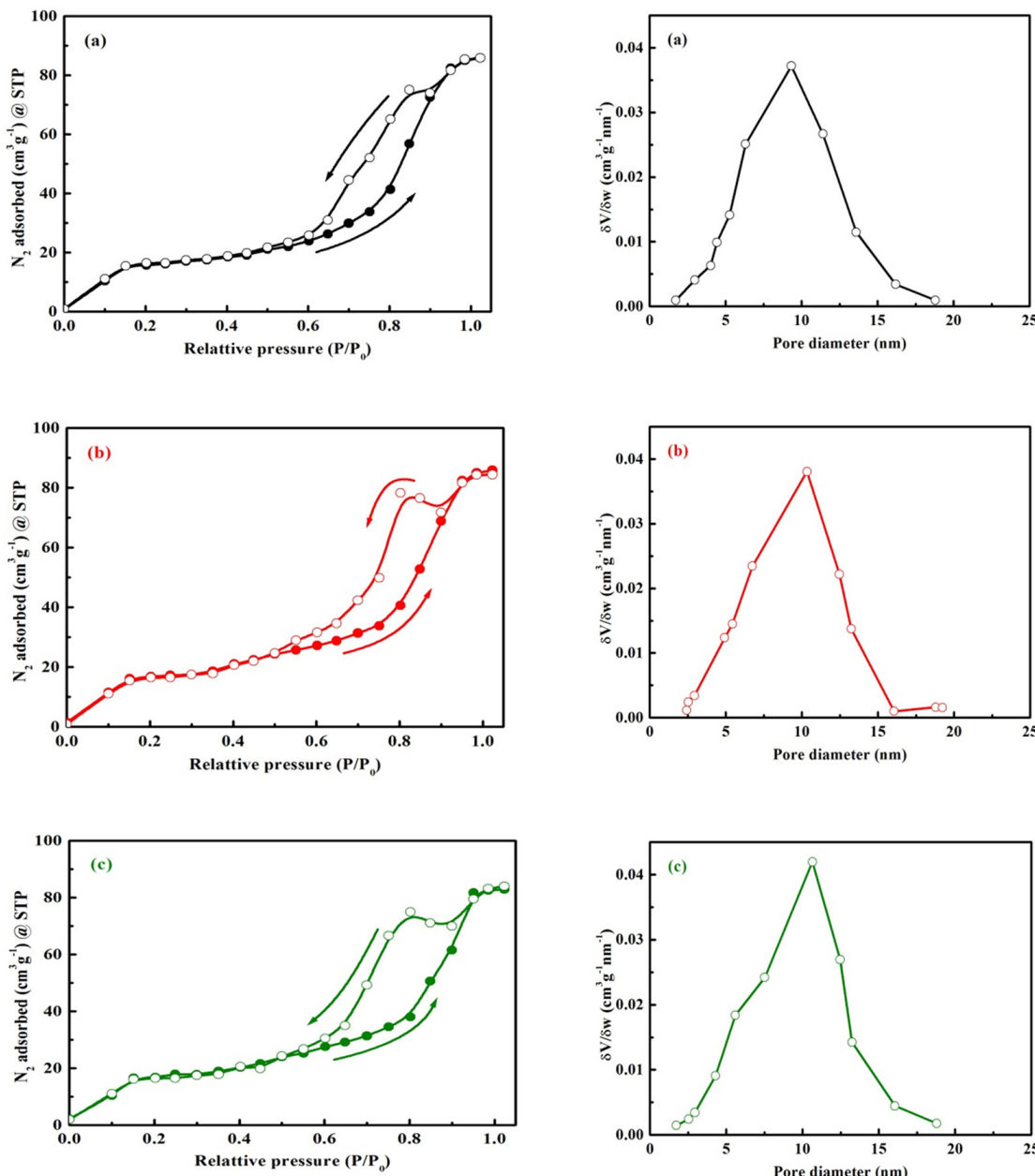


Figure 6. N_2 adsorption–desorption isotherms (left) and pore size distribution curves (right) of $\text{BiFeVO}_{\text{x.y}}$ for (a) $y = 0.03$, (b) $y = 0.07$, and (c) $y = 0.15$.

The estimated values of BET specific surface area (S_{BET}), pore volume, and average pore diameter are summarized in Table 3. It is worthwhile to appoint here that the specific surface area of the mesoporous $\text{BiFeVO}_{\text{x.y}}$ system is nearly 160 times greater than that estimated for the polycrystalline BiNiVO_{x} system synthesized by the solid state reaction [34]. The S_{BET} , pore volume and pore diameter of $\text{BiFeVO}_{\text{x.y}}$ systems were found to be remarkably increased with e content. The significant increment of these microstructural properties

could be attributed to an enhanced coalescence process, since the microwave-assisted calcination is favored by the presence of Fe dopant, which is a good microwave absorber.

Table 3. Specific surface characteristics and dye adsorption efficiencies of BiFeVO_{x,y} photocatalyst series.

<i>y</i>	N ₂ Adsorption-Desorption					MB Adsorption			
	S _{BET} (m ² g ⁻¹)	R ²	Pore Diameter (nm)	Pore Vol. (cm ³ g ⁻¹)	t _e (min)	q _{max} (mg g ⁻¹)	SD	C _e (×10 ⁻⁵ M)	SD (×10 ⁻⁷)
0.03	58.813	0.9948	9.292	0.347	25	15.17	±0.94	3.11	±2.41
0.07	60.348	0.9965	10.345	0.395	25	17.06	±1.12	2.62	±1.83
0.15	65.671	0.9937	10.642	0.448	25	21.52	±1.43	2.31	±1.16

Figure 7 shows the UV-Vis/DR spectra of as-prepared BiFeVO_{x,y} phases. The characteristic absorption edge shifts toward higher wavelengths as the Fe content increases, due to the lowering in the electronic transition energy between the valence band (VB) and conduction band (CB). This is reflected by the variation of optical band-gap energy [14] with the composition (Table 4) as estimated from $(\alpha h\nu)^2$ vs. $h\nu$ plots, depicted as the inset of Figure 7.

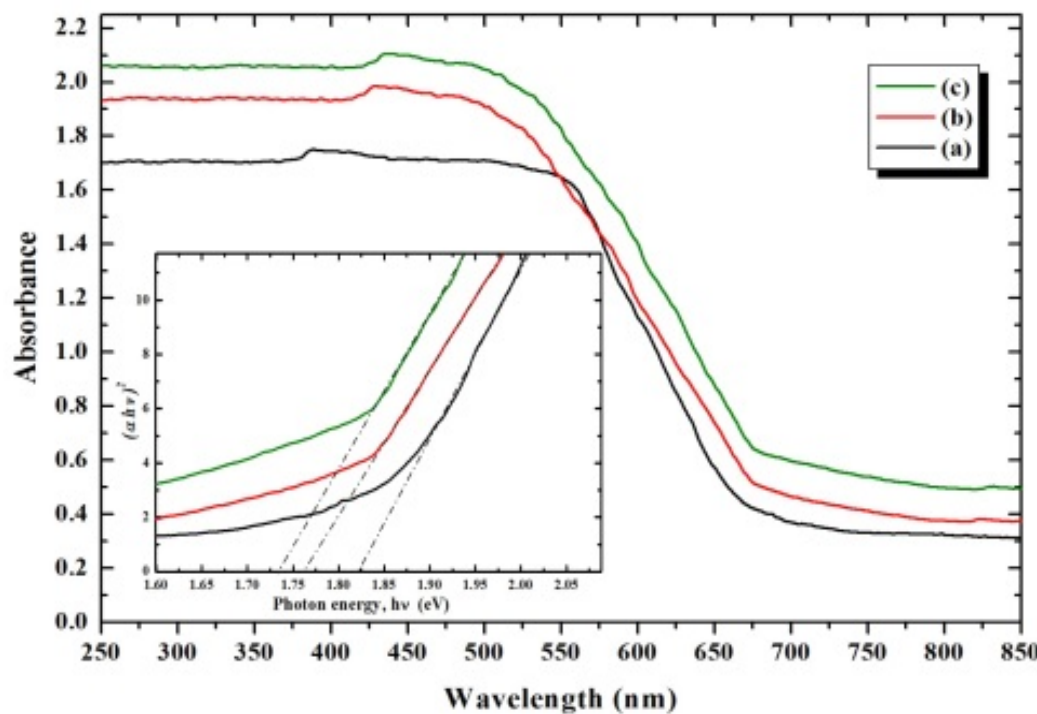


Figure 7. UV-Vis/DR spectra of BiFeVO_{x,y} for (a) $y = 0.03$, (b) $y = 0.07$, and (c) $y = 0.15$. Inset shows $(\alpha h\nu)^2$ vs. $h\nu$ plots.

Table 4. Optical band-gap energies and photocatalytic efficiencies of BiFeVO_{x,y} photocatalyst series.

<i>y</i>	UV-Vis/DR			MB Photodegradation		
	E _g [22]	R ²	SD	k _{app} (min ⁻¹)	R ²	PD%
0.00	2.19	0.9983	±0.019	8.58×10^{-4}	0.9896	10.74
0.03	1.82	0.9966	±0.028	6.05×10^{-3}	0.9987	53.28
0.07	1.76	0.9991	±0.017	0.01142	0.9992	71.92
0.15	1.73	0.9989	±0.021	0.01559	0.9998	84.86

Prior to performing the photocatalytic degradation experiments, it was necessary to determine the equilibrium time and bulk dye concentration for the MB adsorption onto BiFeVO_{x,y} samples in the dark. Figure 8 illustrates the amount of MB adsorbed (q_t) vs. contact time [52] plots for the MB adsorption onto BiFeVO_{x,y} samples (500 mL, 5.0×10^{-5} M + 200 mg BiFeVO_{x,y}), in the dark.

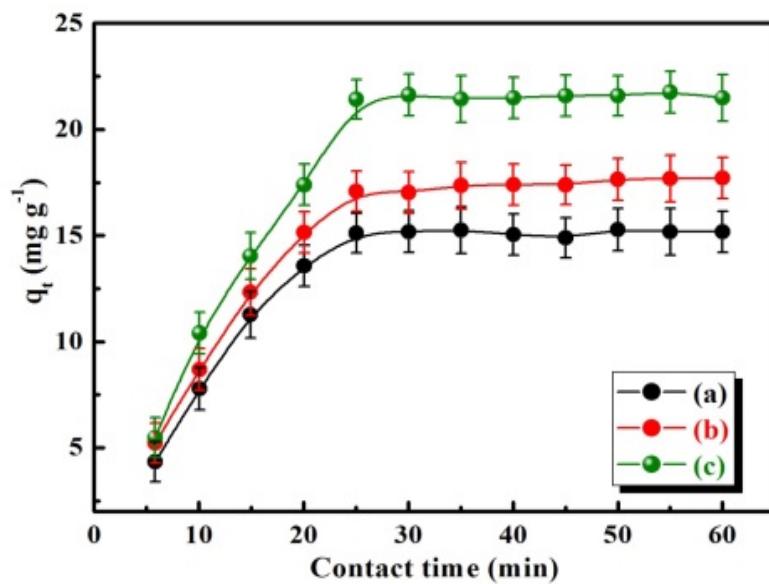


Figure 8. Time- dependence of MB adsorption onto BiFeVO_{x,y} for (a) $y = 0.03$, (b) $y = 0.07$, and (c) $y = 0.15$, in the dark.

It is observed that 25 min was sufficient to reach the adsorption equilibrium. The estimated values of equilibrium time [14], bulk MB concentration [15] and the maximum amount of MB adsorbed at equilibrium (q_{\max}) are listed in Table 3 as the mean \pm SD derived from three replications. The variations of C_e and q_{\max} with Fe content well agree with the results obtained from N₂ desorption isotherms.

The variations of photocatalytic activity of the BiFeVO_{x,y} catalyst series for MB degradation under visible light irradiation in comparison with MB photolysis are illustrated in Figure 9. The values of photocatalytic degradation percent ($PD\%$) after 2 h of irradiation are listed in Table 4.

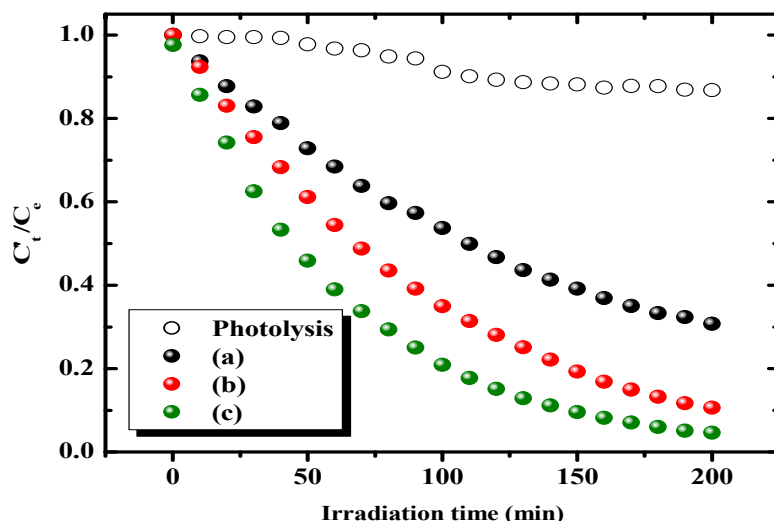


Figure 9. Photocatalytic MB degradation in aqueous medium using BiFeVO_{x,y} catalysts for (a) $y = 0.03$, (b) $y = 0.07$, and (c), $y = 0.15$, under visible light irradiation.

It is observed that the $PD\%$ remarkably increases with Fe dopant content, reaching as much as 84.86% in the presence of the γ -BiFeVO_x.15 phase. The line-regression fitting of $\ln(C_t/C_e)$ vs. irradiation time plots for visible light MB photodegradation catalyzed by the BiFeVO_{x,y} system can be seen in Figure 10.

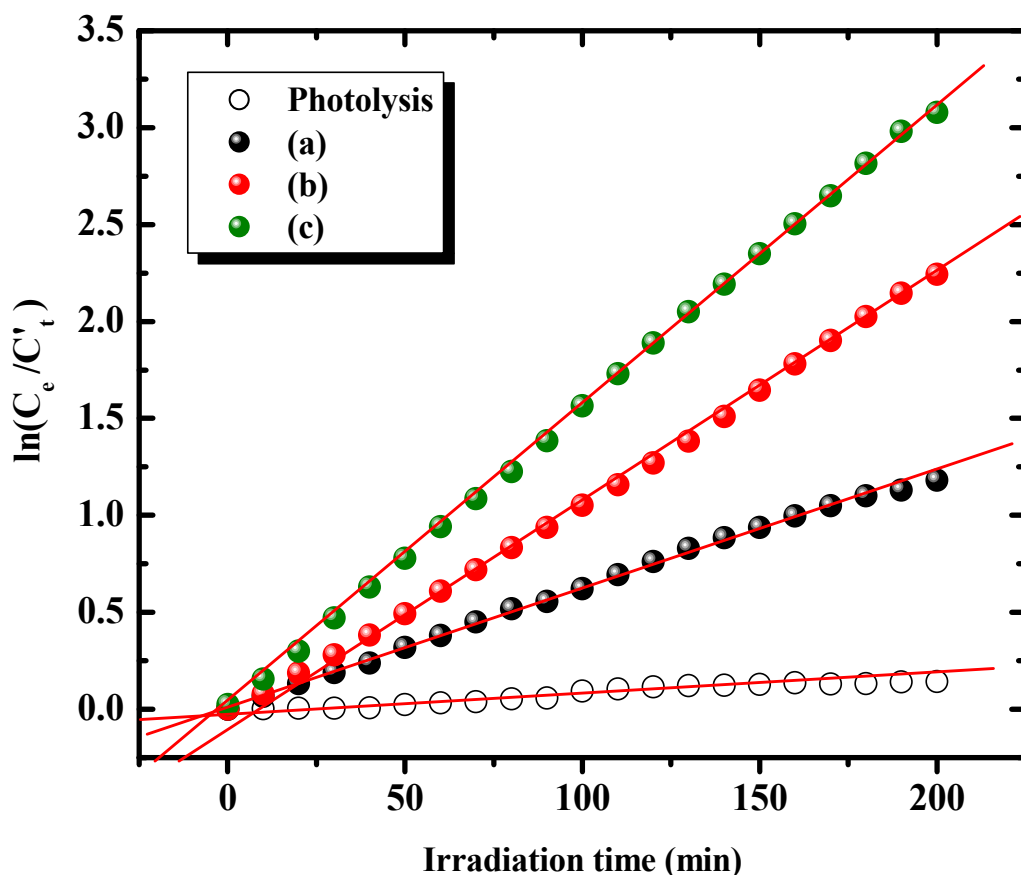


Figure 10. Pseudo first-order kinetics of MB photodegradation catalyzed by BiFeVO_{x,y} for (a) $y = 0.03$, (b) $y = 0.07$, and (c) $y = 0.15$, under visible light irradiation.

The estimated k_{app} values (Table 4) indicate that the photocatalytic MB degradation proceeds more rapidly with β -BiFeVO_x.07 and γ -BiFeVO_x.15 compared with the α -phase, which is consistent with the variation of band-gap energies and surface properties of investigated BiFeVO_{x,y} phases.

The interesting point to be emphasized here is that Bi6s and O2p orbitals of the bis-muthate layers constitute the electronic structure of VB, while that of CB is dominantly composed of V3d and Fe3d orbitals of the perovskite vanadate layers [33,34,53]. Accordingly, the reduction in the band-gap energy of the BiFeVO_{x,y} system with increasing Fe doping is mainly attributed to the additional contribution of Fe3d orbitals in the CB bottom lowering (Figure 11).

This reasonably supports our proposed mechanism for the visible light photocatalytic efficiency of BiMeVO_x materials [34], suggesting the crucial role of highly disordered oxygen vacancies of the perovskite vanadate layers in generating an electron trap under the CB to narrow band gaps. Thus, this occurrence restrains the recombination of photo-generated holes and electrons and consequently improves the visible light photocatalytic activity. Figure 11 presents a summary of the MB degradation photocatalytic reactions upon visible-light irradiation of the BiFeVO_{x,y} system. It is also interesting to note that, in addition to their electronic contribution to the photocatalytic activity, such oxygen vacancies participate, to a great extent, in increasing surface defects/active sites available for the adsorption of more dye molecules, via the synthesis of mesoporous particles [37,54–56].

Therefore, the use of the ethylene glycol–citrate sol–gel method coupled with microwave-assisted calcination in the present study has shown significantly improved photocatalytic efficiencies of synthesized mesoporous nano BiFeVO_{x,y} phases.

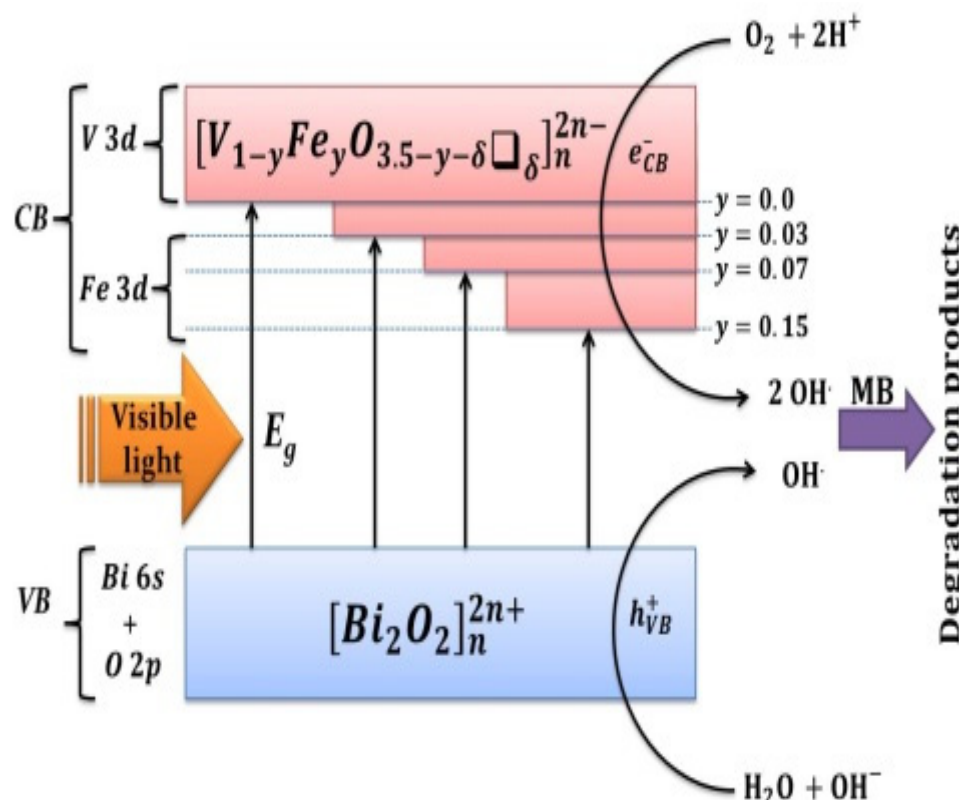


Figure 11. Schematic representation of photocatalytic degradation reactions of MB upon visible-light irradiation of the BiFeVO_{x,y} system.

4. Conclusions

In this work, three BiFeVO_{x,y} mesoporous nanophases were successfully synthesized and tested as visible light photocatalysts. We demonstrated a facile approach for the followed synthesis procedure by ethylene glycol–citrate sol–gel synthesis coupled with microwave-assisted calcination. The highly pronounced photocatalytic efficiency of mesoporous tetragonal γ -BiFeVO₁₅ nanophase indicates that the photocatalytic performance of BiMeVOxes with a layered perovskite structure can be further improved by the doping strategy. Therefore, the combination of doping strategy with such a facile synthesis method played an important role in improving the structure and surface properties of BiFeVO_{x,y} phases and, thereby, enhancing their adsorption and photocatalytic efficiencies. Therefore, the present work proposes a rationalized approach to fabricating and designing potential visible light BiMeVOx-based photocatalysts. However, the photocatalytic degradation mechanism should be proposed and considered in the near future after carrying out advanced trapping experiments of degradation intermediates and final products, along with the reuse of BiFeVO_{x,y} for the photocatalysis.

Author Contributions: Conceptualization, A.A.-A., N.A.S.A.-A. and A.M.A.; methodology, A.A.-A.; software, M.U., A.M.S., S.B. and K.-u.-R.K.; validation, M.U., A.M.S., S.B., S.A.K. and K.-u.-R.K.; formal analysis, A.A.-A., N.A.S.A.-A. and A.M.A.A.; investigation, A.A.-A., N.A.S.A.-A., S.A.K. and A.M.A.A.; resources, M.U., A.M.S., S.B. and K.-u.-R.K.; data curation, A.A.-A. and S.A.K.; writing—original draft preparation, A.A.-A., S.A.K., I.C. and M.U.; writing—review and editing, K.-u.-R.K. and I.C.; visualization, A.A.-A., M.T.E.-S. and M.U.; supervision, N.A.S.A.-A. and R.A.A.; project administration, A.A.-A. and M.T.E.-S.; funding acquisition, M.A.A., A.E.A., A.M.A., M.T.E.-S. and S.A.K. All authors have read and agreed to the published version of the manuscript.

Funding: This work was supported by the National Key R&D Program of China (2021YFA0910800) and the Special Fund for Development of Strategic Emerging Industries in Shenzhen (JCYJ20190808145613154, KQJSCX20180328100801771). Also, the authors extend their appreciation to the deanship of Scientific Research at King Khalid University, Abha KSA for supporting this work under grant number (R.G.P. 2/117/43).

Data Availability Statement: The data presented in this study are available on request from the corresponding author.

Conflicts of Interest: The authors declare no conflict of interest.

References

1. Parsons, S. *Advanced Oxidation Processes for Water and Wastewater Treatment*; IWA Publishing: London, UK, 2004.
2. Rauf, M.A.; Meetani, M.A.; Hisaindee, S. An overview on the photocatalytic degradation of azo dyes in the presence of TiO₂ doped with selective transition metals. *Desalination* **2011**, *276*, 13–27. [[CrossRef](#)]
3. Ali, M.; Hussain, I.; Mehmud, I.; Umair, M.; Hu, S.; Sharif, H.M.A. Recent Breakthroughs and Advancements in NO_x and SO_x Reduction Using Nanomaterials-Based Technologies: A State-of-the-Art Review. *Nanomaterials* **2021**, *11*, 3301. [[CrossRef](#)] [[PubMed](#)]
4. Berbar, Y.; Hammache, Z.E.; Bensaadi, S.; Soukeur, R.; Amara, M.; Van der Bruggen, B. Effect of functionalized silica nanoparticles on sulfonated polyethersulfone ion exchange membrane for removal of lead and cadmium ions from aqueous solutions. *J. Water Process Eng.* **2019**, *32*, 100953. [[CrossRef](#)]
5. Zhang, L.; Wang, L.; Zhang, Y.; Wang, D.; Guo, J.; Zhang, M.; Li, Y. The performance of electrode ultrafiltration membrane bioreactor in treating cosmetics wastewater and its anti-fouling properties. *Environ. Res.* **2022**, *206*, 112629. [[CrossRef](#)] [[PubMed](#)]
6. Shi, C.; Wu, Z.; Yang, F.; Tang, Y. Janus particles with pH switchable properties for high-efficiency adsorption of PPCPs in water. *Solid State Sci.* **2021**, *119*, 106702. [[CrossRef](#)]
7. Bai, B.; Nie, Q.; Wu, H.; Hou, J. The attachment-detachment mechanism of ionic/nanoscale/microscale substances on quartz sand in water. *Powder Technol.* **2021**, *394*, 1158–1168. [[CrossRef](#)]
8. Chen, F.; Ma, J.; Zhu, Y.; Li, X.; Yu, H.; Sun, Y. Biodegradation performance and anti-fouling mechanism of an ICME/electro-biocarriers-MBR system in livestock wastewater (antibiotic-containing) treatment. *J. Hazard. Mater.* **2022**, *426*, 128064. [[CrossRef](#)]
9. Yang, S.S.; Yu, X.L.; Ding, M.Q.; He, L.; Cao, G.L.; Zhao, L.; Ren, N.Q. Simulating a combined lysis-cryptic and biological nitrogen removal system treating domestic wastewater at low C/N ratios using artificial neural network. *Water Res.* **2021**, *189*, 116576. [[CrossRef](#)]
10. Wang, Z.; Lei, Q.; Wang, Z.; Yuan, H.; Cao, L.; Qin, N.; Liu, J. In-situ synthesis of free-standing FeNi-oxyhydroxide nanosheets as a highly efficient electrocatalyst for water oxidation. *Chem. Eng. Sci.* **2020**, *395*, 125180. [[CrossRef](#)]
11. Ge, D.; Yuan, H.; Xiao, J.; Zhu, N. Insight into the enhanced sludge dewaterability by tannic acid conditioning and pH regulation. *Sci. Total Environ.* **2019**, *679*, 298–306. [[CrossRef](#)]
12. Ge, D.; Wu, W.; Li, G.; Wang, Y.; Li, G.; Dong, Y.; Zhu, N. Application of CaO₂-enhanced peroxone process to adjust waste activated sludge characteristics for dewaterability amelioration: Molecular transformation of dissolved organic matters and realized mechanism of deep-dewatering. *Chem. Eng. J.* **2022**, *437*, 135306. [[CrossRef](#)]
13. He, L.; Li, M.X.; Chen, F.; Yang, S.S.; Ding, J.; Ding, L.; Ren, N.Q. Novel coagulation waste-based Fe-containing carbonaceous catalyst as peroxymonosulfate activator for pollutants degradation: Role of ROS and electron transfer pathway. *J. Hazard. Mater.* **2021**, *417*, 126113. [[CrossRef](#)] [[PubMed](#)]
14. Pare, B.; Jonnalagadda, S.B.; Tomar, H.; Singh, P.; Bhagwat, V.W. ZnO assisted photocatalytic degradation of acridine orange in aqueous solution using visible irradiation. *Desalination* **2008**, *232*, 80–90. [[CrossRef](#)]
15. Daneshvar, N.; Salari, D.; Khataee, A.R. Photocatalytic degradation of azo dye acid red 14 in water: Investigation of the effect of operational parameters. *J. Photochem. Photobiol. A Chem.* **2003**, *157*, 111–116. [[CrossRef](#)]
16. Guo, R.; Yu, L.; Liu, Z.; Pan, J.; Yao, Y.; Liu, L. Enthalpy induced phase partition toward hierarchical, nanostructured high-entropy alloys. *Nano Res.* **2021**, *1*–9. [[CrossRef](#)]
17. Zhang, M.; Sun, X.; Wang, C.; Wang, Y.; Tan, Z.; Li, J.; Xi, B. Photocatalytic degradation of rhodamine B using Bi₄O₅Br₂-doped ZSM-5. *Mater. Chem. Phys.* **2022**, *278*, 125697. [[CrossRef](#)]
18. Cheng, J.Z.; Tan, Z.R.; Xing, Y.Q.; Shen, Z.Q.; Zhang, Y.J.; Liu, L.L.; Liu, S.Y. Exfoliated conjugated porous polymer nanosheets for highly efficient photocatalytic hydrogen evolution. *J. Mater. Chem.* **2021**, *9*, 5787–5795. [[CrossRef](#)]
19. Mahmoodi, N.M.; Arami, M.; Limaei, N.Y. Photocatalytic degradation of triazinic ring-containing azo dye (Reactive Red 198) by using immobilized TiO₂ photoreactor: Bench scale study. *J. Hazard. Mater.* **2006**, *133*, 113–118. [[CrossRef](#)]
20. Yawalkar, A.A.; Bhatkhande, D.S.; Pangarkar, V.G.; Beenackers, A.A.C.M. Solar-assisted photochemical and photocatalytic degradation of phenol. *J. Chem. Technol. Biotechnol.* **2001**, *76*, 363–370. [[CrossRef](#)]
21. Legrini, O.; Oliveros, E.; Braun, A.M. Photochemical processes for water treatment. *Chem. Rev.* **1993**, *93*, 671–698. [[CrossRef](#)]
22. Liu, Y.; Zhang, Q.; Yuan, H.; Luo, K.; Li, J.; Hu, W.; Bazaka, K. Comparative study of photocatalysis and gas sensing of ZnO/Ag nanocomposites synthesized by one-and two-step polymer-network gel processes. *J. Alloys Compd.* **2021**, *868*, 158723. [[CrossRef](#)]

23. Konstantinou, I.K.; Albanis, T.A. TiO₂-assisted photocatalytic degradation of azo dyes in aqueous solution: Kinetic and mechanistic investigations: A review. *Appl. Catal. B Environ.* **2004**, *49*, 1–14. [CrossRef]
24. You, J.; Liu, C.; Feng, X.; Lu, B.; Xia, L.; Zhuang, X. In situ synthesis of ZnS nanoparticles onto cellulose/chitosan sponge for adsorption–photocatalytic removal of Congo red. *Carbohydr. Polym.* **2022**, *288*, 119332. [CrossRef]
25. Li, G.; Huang, S.; Zhu, N.; Yuan, H.; Ge, D. Near-infrared responsive upconversion glass-ceramic@ BiOBr heterojunction for enhanced photodegradation performances of norfloxacin. *J. Hazard. Mater.* **2021**, *403*, 123981. [CrossRef] [PubMed]
26. Di Paola, A.; García-López, E.; Marci, G.; Palmisano, L. A survey of photocatalytic materials for environmental remediation. *J. Hazard. Mater.* **2012**, *211*, 3–29. [CrossRef]
27. Duan, Y.; Liu, Y.; Chen, Z.; Liu, D.; Yu, E.; Zhang, X.; Du, H. Amorphous molybdenum sulfide nanocatalysts simultaneously realizing efficient upgrading of residue and synergistic synthesis of 2D MoS₂ nanosheets/carbon hierarchical structures. *Green Chem.* **2020**, *22*, 44–53. [CrossRef]
28. Al-Areqi, N.A.; Beg, S. Studies in composition and temperature dependence of phase stability in the Bi₄Ag_xV_{2-x}O_{11-(2x)-δ} system and their influence on the oxide ion performance. *Phase Transit.* **2012**, *85*, 255–263. [CrossRef]
29. Al-Areqi, N.A.; Beg, S.; Al-Alas, A. Study on phase stability and oxide ion conductivity in the BIAGVOX system. *J. Phys. Chem. Solids* **2012**, *73*, 730–734. [CrossRef]
30. Beg, S.; Al-Areqi, N.A.; Ghaleb, K.A.; Al-Alas, A.; Hafeez, S. Effect of Ni (II) substitution on phase stabilization electrical properties of BICo (III) VO_x. 20 oxide-ion conductor. *Philos. Mag.* **2014**, *94*, 1661–1673. [CrossRef]
31. Jia, J.S.; Cao, Y.; Wu, T.X.; Tao, Y.; Pan, Y.M.; Huang, F.P.; Tang, H.T. Highly regio-and stereoselective markovnikov hydrosilylation of alkynes catalyzed by high-nuclearity {Co14} Clusters. *ACS Catal.* **2021**, *11*, 6944–6950. [CrossRef]
32. Duan, Y.; Fu, H.; Zhang, L.; Gao, R.; Sun, Q.; Chen, Z.; Du, H. Embedding of ultra-dispersed MoS₂ nanosheets in N, O heteroatom-modified carbon nanofibers for improved adsorption of Hg₂₊. *Compos. Commun.* **2022**, *31*, 101106. [CrossRef]
33. Thakral, V.; Uma, S. Investigation of visible light photocatalytic behavior of Bi₄V₂O₁₁₋δ and BIMEVOX (ME = Al, Ga) oxides. *Mater. Res. Bull.* **2010**, *45*, 1250–1254. [CrossRef]
34. Al-Areqi, N.A.; Al-Alas, A.; Al-Kamali, A.S.; Ghaleb, K.A.; Al-Mureish, K. Photodegradation of 4-SPPN dye catalyzed by Ni (II)-substituted Bi₂VO₅. 5 system under visible light irradiation: Influence of phase stability and perovskite vanadate–oxygen vacancies of photocatalyst. *J. Mol. Catal. A Chem.* **2014**, *381*, 1–8. [CrossRef]
35. Hu, X.; Zhang, P.; Wang, D.; Jiang, J.; Chen, X.; Liu, Y.; Li, P. AIEgens enabled ultrasensitive point-of-care test for multiple targets of food safety: Aflatoxin B1 and cyclopiazonic acid as an example. *Biosens. Bioelectron.* **2021**, *182*, 113188. [CrossRef] [PubMed]
36. Chen, C.X.; Yang, S.S.; Ding, J.; Wang, G.Y.; Zhong, L.; Zhao, S.Y.; Ren, N.Q. Non-covalent self-assembly synthesis of AQ2S@ rGO nanocomposite for the degradation of sulfadiazine under solar irradiation: The indispensable effect of chloride. *Appl. Catal. B Environ.* **2021**, *298*, 120495. [CrossRef]
37. Chen, X.; Liu, J.; Wang, H.; Ding, Y.; Sun, Y.; Yan, H. One-step approach to novel Bi₄V₂O₁₁ hierarchical hollow microspheres with high visible-light-driven photocatalytic activities. *J. Mater. Chem.* **2012**, *2013*, 877.
38. Li, G.; Huang, S.; Zhu, N.; Yuan, H.; Ge, D.; Wei, Y. Defect-rich heterojunction photocatalyst originated from the removal of chloride ions and its degradation mechanism of norfloxacin. *Chem. Eng. J.* **2021**, *421*, 127852. [CrossRef]
39. He, H.; Zhu, Q.Q.; Yan, Y.; Zhang, H.W.; Han, Z.Y.; Sun, H.; Du, M. Metal–organic framework supported Au nanoparticles with organosilicone coating for high-efficiency electrocatalytic N₂ reduction to NH₃. *Appl. Catal. B Environ.* **2022**, *302*, 120840. [CrossRef]
40. Al-Alas, A.; Beg, S.; Al-Areqi, N.A.; Hafeez, S. Influence of microwave-assisted calcination on structural properties and oxide-ion performance of layered-perovskite γ-BIMVOX solid electrolyte synthesized by ethylene glycol–citrate sol–gel route. *J. Eur. Ceram. Soc.* **2013**, *33*, 2111–2117. [CrossRef]
41. Bouhlali, E.D.T.; Bammou, M.; Sellam, K.; El Midaoui, A.; Bourkhis, B.; Ennassir, J.; Filali-Zegzouti, Y. Physicochemical properties of eleven monofloral honey samples produced in Morocco. *Arab J. Basic Appl. Sci.* **2019**, *26*, 476–487. [CrossRef]
42. Alga, M.; Ammar, A.; Essalim, R.; Tanouti, B.; Mauvy, F.; Decourt, R. Synthesis, sintering and electrical properties of P-doped Bi₄V₂O₁₁ ceramics. *Solid State Sci.* **2005**, *7*, 1173–1179. [CrossRef]
43. Abraham, F.; Boivin, J.C.; Mairesse, G.; Nowogrocki, G. The BIMEVOX series: A new family of high performances oxide ion conductors. *Solid State Ion.* **1990**, *40*, 934–937. [CrossRef]
44. Pernot, E.; Anne, M.; Bacmann, M.; Strobel, P.; Fouletier, J.; Vannier, R.N.; Nowogrocki, G. Structure and conductivity of Cu and Ni-substituted Bi₄V₂O₁₁ compounds. *Solid State Ion.* **1994**, *70*, 259–263. [CrossRef]
45. Beg, S.; Al-Areqi, N.A.S. Structural and electrical study of CeIV-substituted bismuth vanadate. *J. Phys. Chem. Solids* **2009**, *70*, 1000–1007. [CrossRef]
46. Tripathy, D.; Saikia, A.; Tado, G.T.; Pandey, A. Role of Al and Ti doping in modulating electrical properties of BIVOX system. *J. Adv. Ceram.* **2019**, *8*, 489–499. [CrossRef]
47. Abrahams, I.; Krok, F. Defect chemistry of the BIMEVOXes. *J. Mater. Chem.* **2002**, *12*, 3351–3362. [CrossRef]
48. Boivin, J.C.; Mairesse, G. Recent material developments in fast oxide ion conductors. *Chem. Mater.* **1998**, *10*, 2870–2888. [CrossRef]
49. Abrahams, I.; Krok, F.; Nelstrop, J.A.G. Defect structure of quenched γ-BICOVOX by combined X-ray and neutron powder diffraction. *Solid State Ion.* **1996**, *90*, 57–65. [CrossRef]
50. Liang, C.; Liu, C.; Li, F.; Wu, F. The effect of praseodymium on the adsorption and photocatalytic degradation of azo dye in aqueous Pr³⁺-TiO₂ suspension. *Chem. Eng. J.* **2009**, *147*, 219–225. [CrossRef]

51. Cao, G.; Li, Y.; Zhang, Q.; Wang, H. Synthesis and characterization of $\text{La}_2\text{O}_3/\text{TiO}_{2-x}\text{F}_x$ and the visible light photocatalytic oxidation of 4-chlorophenol. *J. Hazard. Mater.* **2010**, *178*, 440–449. [[CrossRef](#)]
52. Orlowska, M.; Koutchma, T.; Kostrzynska, M.; Tang, J.; Defelice, C. Evaluation of mixing flow conditions to inactivate *Escherichia coli* in opaque liquids using pilot-scale Taylor–Couette UV unit. *J. Food Eng.* **2014**, *120*, 100–109. [[CrossRef](#)]
53. Lv, K.; Li, J.; Qing, X.; Li, W.; Chen, Q. Synthesis and photo-degradation application of WO_3/TiO_2 hollow spheres. *J. Hazard. Mater.* **2011**, *189*, 329–335. [[CrossRef](#)] [[PubMed](#)]
54. Jiang, Z.; Liu, Y.; Li, M.; Jing, T.; Huang, B.; Zhang, X.; Dai, Y. One-pot solvothermal synthesis of $\text{Bi}_4\text{V}_2\text{O}_{11}$ as a new solar water oxidation photocatalyst. *Sci. Rep.* **2016**, *6*, 22727. [[CrossRef](#)]
55. Umair, M.; Jabbar, S.; Sultana, T.; Ayub, Z.; Abdelgader, S.A.; Zhu, X.; Zhang, C.; Lu, F.; Bie, X.; Lu, Z. Chirality of the biomolecules enhanced its stereospecific action of dihydromyricetin enantiomers. *Food Sci. Nutr.* **2020**, *8*, 4843–4856. [[CrossRef](#)] [[PubMed](#)]
56. Muhammad, U.; Zhu, X.; Lu, Z.; Han, J.; Sun, J.; Tayyaba, S.; Abbasi, B.; Siyal, F.A.; Dhama, K.; Saqib, J. Effects of extraction variables on pharmacological activities of vine tea extract (*Ampelopsis grossedentata*). *Int. J. Pharmacol.* **2018**, *14*, 495–505. [[CrossRef](#)]